

## Materials processing at atmospheric pressure: Nonequilibrium effects on nanotechnology and mega-industries\*

Tomohiro Nozaki<sup>‡</sup> and Ken Okazaki

*Department of Mechanical and Control Engineering, Tokyo Institute of Technology, 2-12-1 O-okayama, Meguro, Tokyo, 1528552, Japan*

*Abstract:* Applications of atmospheric pressure nonequilibrium plasmas, because of their special advantages of forming reactive plasmas in a simple reactor, are spreading into various engineering fields, not only of materials processing, but also into energy and environment areas. Our group has explored new applications of both filamentary and diffuse barrier discharges, including the establishment of appropriate modeling, which enables better optimization of given plasma processes. More recently, microplasmas produced in submillimeter to micrometer reactors are also highlighted in association with atmospheric pressure nonequilibrium plasma because such small-scale plasmas frequently require high-density media to produce. This paper overviews our recent projects: (1) steam reforming of methane using filamentary barrier discharge; (2) deposition of carbon nanotubes in atmospheric pressure radio frequency discharge (APRFD); and (3) synthesis of silicon nanoparticles using microplasma.

*Keywords:* plasma; nanotechnology; microplasma; filamentary barrier discharges; glow discharges; reforming; atmospheric pressure nonequilibrium plasma; atmospheric pressure CVD; collisional sheath; nanoparticles.

### INTRODUCTION

Atmospheric pressure nonequilibrium plasma is recognized as weakly ionized low-temperature plasma from the fact that its electron temperature is much higher than its gas temperature. This type of plasma has been produced in filamentary dielectric barrier discharge known as DBD. It has been used historically in the ozone industry since 1857 [1]. Now, DBD is recognized as a viable processing plasma for chemical conversion processes. Its applications are spreading into many fields, such as gas cleaning and fuel reforming, because of the growing concern of the global environment. In the late 1980s, S. Okazaki and coworkers developed atmospheric pressure DBD, in which they propose atmospheric pressure glow discharge (APGD), providing spatially uniform nonequilibrium plasma at atmospheric pressure [2]. Research activities and applications in this new field of plasma science and technology have been expanding not only into gas treatments, but also surface modification, coating, and chemical vapor deposition (CVD) [3–5]. The primary interest of APGD has been emphasized in practical applications because it minimizes the needs for vacuum systems and enables the handling of bulky materials in a continuous process. It even allows direct injection of liquid precursors to deposit various thin films.

---

\*Paper presented at the 17<sup>th</sup> International Symposium on Plasma Chemistry (ISPC 17), Toronto, Ontario, Canada, 7–12 August 2005. Other presentations are published in this issue, pp. 1093–1298.

<sup>‡</sup>Corresponding author

From a fundamental viewpoint, a broad range of operating pressures from  $10^{-1}$  to  $10^5$  Pa might provide a comprehensive understanding of fundamental processes in both gas phase and boundary phenomena in plasma materials processing: It is believed that it will create greater value-added plasma processing in various industries where existing low-pressure plasmas are currently too expensive to introduce. Atmospheric pressure nonequilibrium plasmas have shown remarkable progress in formation techniques in the field of microplasma [6]. Efficient generation methods and diagnostics of microplasma are being investigated, along with the development of new applications including light sources of ultra-short wavelengths, three-dimensional micromachining tools, and other plasma devices. In addition to barrier discharges and microplasma, various types of atmospheric pressure nonequilibrium plasma sources are available to develop desired processes [1,7,8].

This paper provides an overview of materials processing in atmospheric pressure nonequilibrium plasmas based on our recent work. Section 2 introduces fundamental characteristics of both filamentary and diffuse barrier discharges. This paper designates filamentary barrier discharge as dielectric barrier discharge (DBD), and diffuse barrier discharge as atmospheric pressure glow discharge (APGD), but both are actually DBDs. Optical emission spectroscopy, energy balance analysis, and gas chromatographic analysis are provided to distinguish DBD and APGD. In section 3, we introduce atmospheric pressure radio frequency discharge (APRFD) to distinguish it from APGD because radio frequency operation no longer requires a dielectric barrier between metallic electrodes to maintain a spatially uniform discharge at atmospheric pressure [4]. Novel applications DBD, APRFD, and microplasma are introduced briefly in section 3: (1) low-temperature fuel reforming using filamentary barrier discharge, (2) deposition of carbon nanotubes in APRFD, and (3) creation of microplasma and application to the synthesis of silicon nanoparticles. Finally, concluding remarks are presented.

## THERMAL STRUCTURE OF FILAMENTARY AND DIFFUSE BARRIER DISCHARGES

Both filamentary and diffuse barrier discharges are characterized as weakly ionized plasma with properties resembling transient high-pressure glow discharge. The immediate termination of developing plasma as a result of the charge built up on dielectric material realizes highly reactive nonequilibrium conditions at atmospheric pressures. On the other hand, the electrical energy put into atmospheric pressure plasma is readily transformed into thermal energy via a large number of particle collisions that might lead to severe gas heating. The energy efficiency of material conversion in those plasma processes is normally less than 10 %. From this perspective, we analyzed energy distribution mechanisms in methane-fed DBD and APGD by focusing on energy balance analysis, emission spectroscopy of the rotational band of CH ( $((0,0) A^2\Delta \rightarrow X^2\Pi)$ ), and gas chromatographic analysis [9,10]. We also analyzed thermal structure of DBD and APGD by specifically examining gas temperature profiles across the discharge gap. Detailed electrical and optical measurements, as well as computer modeling of DBD [11,12] and APGD [13], have been presented elsewhere.

## Voltage-current waveforms and emission distribution of barrier discharges

A peculiarity of DBD is the presence of a dielectric insulator on one or both metallic electrodes, which leads to formation of numerous filamentary microdischarges of nanosecond duration. Figure 1 shows typical voltage and current waveforms that are observed in methane-fed DBD. It also shows a photograph of streamers taken with a high-speed intensified charge-coupled device (CCD) camera with 10-ns exposure time (i-Star DH712; Andor Technology). Numerous nanosecond current pulses are observed at every half cycle of applied voltage. The immediate termination of the developing discharge as a result of the charge built up on the dielectric barrier creates a highly reactive nonequilibrium condition at atmospheric pressure. Because of the charge accumulation on the barrier, microdischarges are dispersed randomly between the electrodes. Each filament corresponds to a nanosecond current pulse that appears in the current waveform.

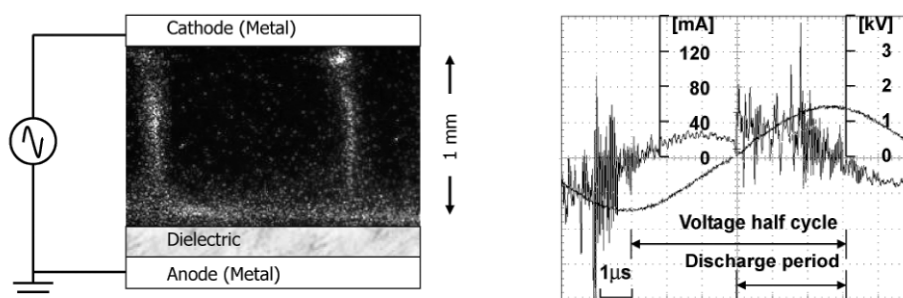


**Fig. 1** Photograph of a single streamer produced in pure methane at 20 °C (10-ns exposure time), and voltage and current waveforms in DBD (80 kHz AC).

Figure 2 shows 80 kHz AC high voltage, and current waveforms obtained in atmospheric pressure diffuse barrier discharge in which S. Okazaki and coworkers designated it as APGD [2]. The APGD in Fig. 2 was produced in an identical barrier discharge reactor and power source shown in Fig. 1. The only difference is that the feed gas is diluted by helium. With a minimum over-voltage, a single current pulse with 500 ns duration appeared at every half cycle of the voltage. Corresponding emission distributions in the visible spectrum are described in Figs. 2a–2b. Figure 2a shows discharge events synchronized with negative discharge current with 1- $\mu$ s exposure time (metallic cathode–dielectric anode). Figure 2b was recorded during positive discharge current. Emission distribution is not localized in the radial direction, but intense emission layer is created near the temporary cathode in both pictures. The emission distribution of APGD has a structure that is similar to that of low-pressure glow discharge at the time when a single current pulse reaches its maximum [14]. At this moment, electron density in the temporary cathode layers can reach  $10^{11} \text{ cm}^{-3}$  [14,15]. Production of metastable-state helium by electron impact and associated Penning ionization becomes an important source of secondary electrons. The electron avalanche does not transform into streamer because the operating voltage is sufficiently lower in helium, and a glow-like discharge would mostly take place.

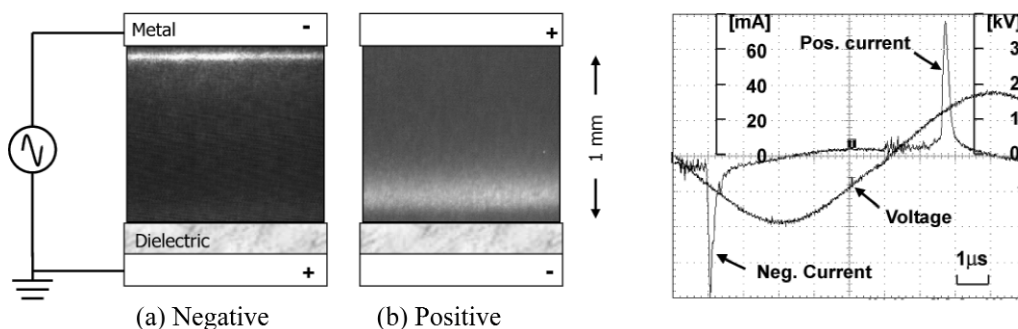


**Fig. 2** Voltage and current waveforms in APGD (80 kHz AC) and photographs of APGD synchronized with (a) negative discharge current, (b) positive discharge current with 1- $\mu$ s exposure time. A mixture of helium and methane (He: CH<sub>4</sub> = 98: 2) at 20 °C.

### Relationship between rotational temperature and gas temperature

Figures 1 and 2 show that feed gas breaks down repeatedly at regular intervals. Therefore, the following relation can express the net temperature increase in the gap.

$$\Delta T_{\text{net}} \approx (T_{\text{rot}} - T_0) \approx \Delta T_{\text{ave}} + \Delta T_{\text{plasma}} \text{ [K]} \quad (1)$$

Here,  $T_{\text{net}}$  represents the net temperature increase in the gap,  $T_{\text{rot}}$  refers to the rotational temperature,  $T_0$  is the initial temperature of incoming gas,  $\Delta T_{\text{ave}}$  represents time- and space-averaged temperature increase of feed gas, and  $\Delta T_{\text{plasma}}$  is the local and temporal temperature increase attributable to microdischarge or glow discharge formation. The rotational temperature was derived by the Boltzmann plot of rotational band of CH emission [9,16]. The average temperature increase ( $\Delta T_{\text{ave}}$ ) was determined using the balance of discharge power, which is not used for methane decomposition (endothermic reaction) and heat removal to both electrodes [10,17]. On the other hand,  $\Delta T_{\text{plasma}}$  is the local and temporal gas temperature increase resulting from formation of transient discharges. To characterize the thermal structure of DBD and APGD, we must evaluate the individual contribution of  $\Delta T_{\text{ave}}$  and  $\Delta T_{\text{plasma}}$  to the net temperature increase ( $\Delta T_{\text{net}}$ ).

Rotational temperature vs. initial gas temperature (see eq. 1) in methane-fed DBD is shown in Fig. 3 [10]. Rotational temperature is 100–150 K higher than the initial gas temperature because microdischarges are localized in a narrow filamentary region, but it showed sufficient sensitivity to the variation of the initial gas temperature. The results shown here are much higher than those provided by Luque et al. [18] as predicted by Kogelschatz [19]. They concluded that the temperature increase in microdischarges is about 15–45 K in  $\text{CH}_4/\text{CO}_2$  barrier discharges, which are operated by 14 kHz pulsed voltage (FWHM: ca. 2  $\mu\text{s}$ ). Comparison of these two conclusions suggests an important aspect. High-frequency operation conducted in our experiment (80 kHz) induces microdischarges that excessively heat discharge channels. Increasing frequency in filamentary discharge mode induces a strong memory effect in which microdischarges are not dispersed well. The energy density in the remaining conductive channel, on average, increases as the number of discharge events increases during the “lifetime” of microdischarges. It was further investigated in DBD and APGD by specifically investigating the energy balance and heat transfer [10,20]. Excess temperature increase in DBD (ca. 100 K) was also observed with respect to input power and gas velocity, as shown in Figs. 4 and 5. The rotational temperature in APGD is fairly close to the average gas temperature because the diffuse discharge decreases the power density. From Figs. 3 to 5,  $\Delta T_{\text{plasma}}$  in filamentary mode is nearly constant, regardless of the initial gas temperature (300–400 K), input power (0.5–3.8  $\text{W cm}^{-2}$ ), and gas velocity (1–6  $\text{m s}^{-1}$ ) insofar as gas gap (0.5 mm), dielectrics (0.5 mm Pyrex), and pressure were unchanged. Raising the input power for a given configuration simply increases a number of microdischarges per unit area of the electrode surface, whereas energy spent in an individual microdischarge, on average, does not change markedly. On the other hand,  $\Delta T_{\text{ave}}$  depends mostly on the input power and external cooling conditions: It approaches zero at zero input power (see Fig. 4).

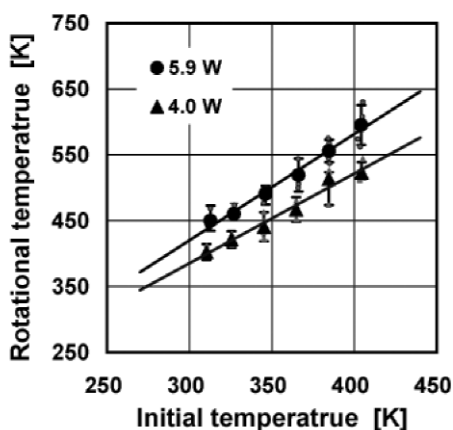


**Fig. 3** Rotational temperature vs. initial gas temperature in DBD. Discharge area;  $10 \times 80 \text{ mm}^2$ , gap; 0.5 mm, dielectric; 0.5 mm Pyrex, gas velocity,  $1.0 \text{ m s}^{-1}$ , and 80 kHz AC.

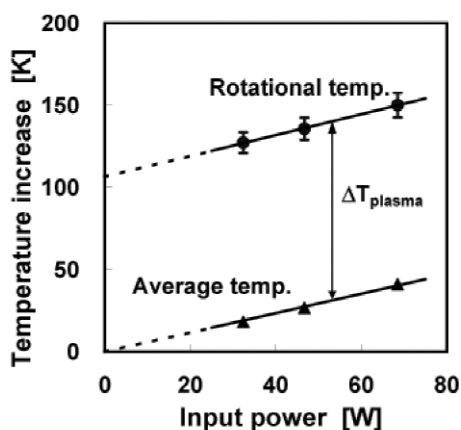


**Fig. 4** Comparison between average gas temperature and rotational temperature in DBD. Discharge conditions: see Fig. 3.

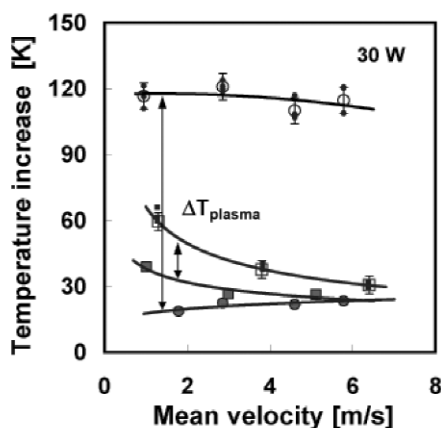


**Fig. 5** Average temperature for (●) DBD and (■) APGD. Rotational temperature for (○) DBD and (□) APGD. Discharge conditions: see Fig. 3.

### Distribution of net temperature increase across discharge gap ( $\Delta T_{\text{ave}} + \Delta T_{\text{plasma}}$ )

As a practical matter, net temperature increase ( $\Delta T_{\text{ave}} + \Delta T_{\text{plasma}}$ ) also poses important issues. Figure 6a shows the net temperature increase in DBD obtained using 80 kHz AC high voltage. When increasing input power, the net temperature increase ( $\Delta T_{\text{net}}$ ) in the middle of the gap increases remarkably because of poor cooling conditions. The net gas temperature does not approach the electrode temperature (20 °C), even when decreasing input power to zero, because energy spent in microdischarges does not continuously approach zero with decreasing input power. Consequently, gas temperature increases on both electrodes should correspond to  $\Delta T_{\text{plasmae}}$ . In fact,  $\Delta T_{\text{plasmae}}$  (ca. 100 K), which is shown in Fig. 4, corresponds to the temperature increase on both electrodes (Fig. 6a). In addition, these temperatures are uniquely independent of the input power.  $\Delta T_{\text{ave}}$  can be minimized by improving the external cooling condition of the reactor. However, the memory effect attributable to high-frequency operation induces considerable gas heating, which reached 100–150 K higher than the initial gas temperature. In APGD, the net temperature increase near the metallic electrode is remarkable, as shown in Fig. 6b, and significantly increases with input power. Temperature distribution is broadened by heat conduction through gas media (main component is helium).

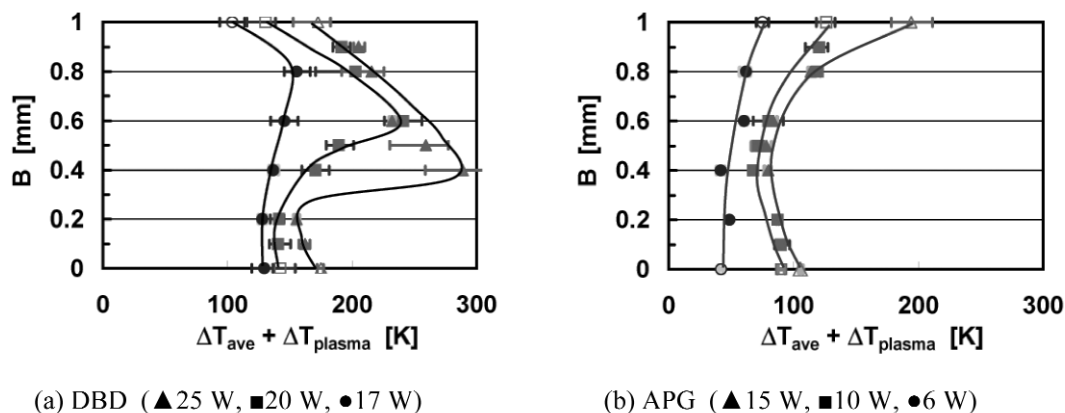


Fig. 6 Net temperature distribution in DBD and APGD. As for reactor configurations, see Fig. 1 for DBD and Fig. 2 for APGD, respectively.

## APPLICATIONS

### Low-temperature fuel reforming using filamentary barrier discharge

Although industrial applications of  $C_1$  chemistry depend mostly on catalytic conversion processes, plasma catalysis is highlighted as a unique technique for energy-saving and environment-safe purposes with increasing demand of hydrogen and synthesis gas [21–23]. More recently, atmospheric pressure nonthermal plasmas such as Plasmatron [24] and Glidarc [25,26] are recognized as economically competitive plasma fuel converters. Electrical energy consumption of those plasma reactors is normally less than 10 % of heating value of the initial feedstock when those plasmas are combined with partial oxidation. The driving force of the reforming reaction relies essentially on heat released by partial oxidation, whereas the plasma preliminary enhances the combustion process of initial fuel and air mixture in a wide range of operating conditions.

We have developed a DBD and catalyst hybrid reactor for combustion-free, low-temperature steam reforming of methane [27,28]. This technique allows utilization of low-temperature thermal energy wasted from various industries, which eventually provides various energy utility options. The idea behind the project is that low-calorific fuels such as biogas can be upgraded in the temperature range of 300–500 °C, which corresponds to the exhaust gas from an internal combustion engine, by the help of nonequilibrium plasma. The resulting hydrogen-enriched biogas improves the ignition stability and is then available to drive an internal combustion engine.

Figure 7 illustrates the configuration of DBD and catalyst hybrid reactor. The basic idea of the hybrid reactor was first proposed by Mizuno and Yamamoto [29,30]. The rod-to-tube ( $\phi_r$  3 mm  $\times$   $\phi_t$  20 mm) reactor was packed with catalyst pellets of 12 wt % Ni/ $\gamma$ - $Al_2O_3$  (3 mm) in the volume of  $\phi_t$  20  $\times$  50 mm. Bipolar pulsed voltage ( $\pm$ 20 kV at 1–5 kpps with FWHM: ca. 2  $\mu$ s) was applied between the center and external ground electrode. The discharge is ignited at pellet contacts. It then propagates, thereby covering the pellet surface and providing the best interaction between plasma and catalyst. We used simulated biogas, which includes 60 % methane and 40 % nitrogen ( $CH_4:N_2 = 6:4$ ). The steam and methane ratio ( $S/C$ ) was set to one ( $S/C = H_2O/CH_4 = 1$ ). The plasma hybrid process must convert 20 % of initial methane that enriches hydrogen in output gas by 32 % (dry base). It remarkably enhances the combustibility of poor biogas and can drive an internal combustion engine.

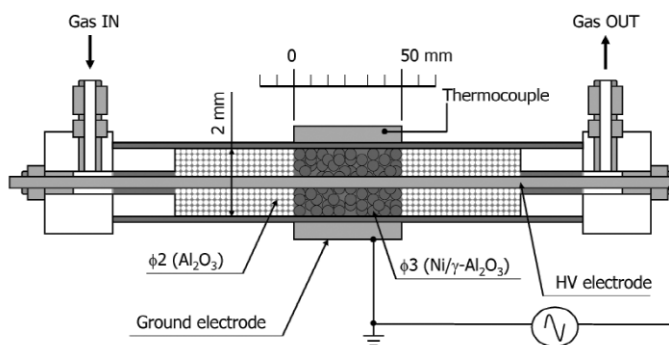
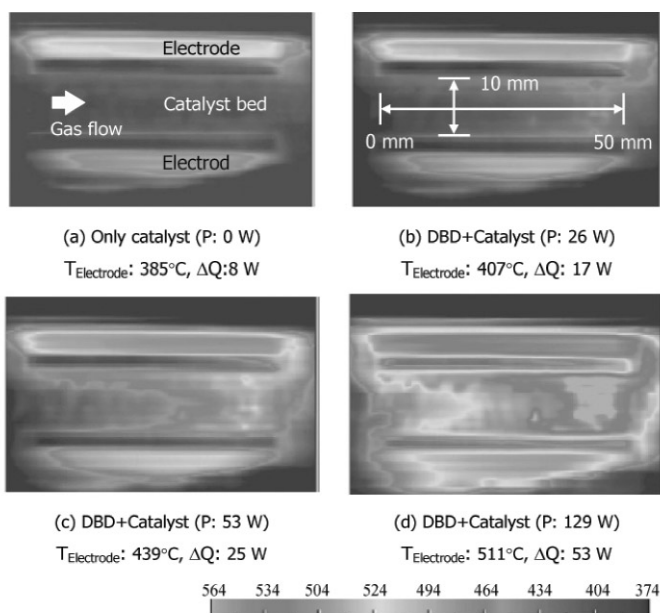
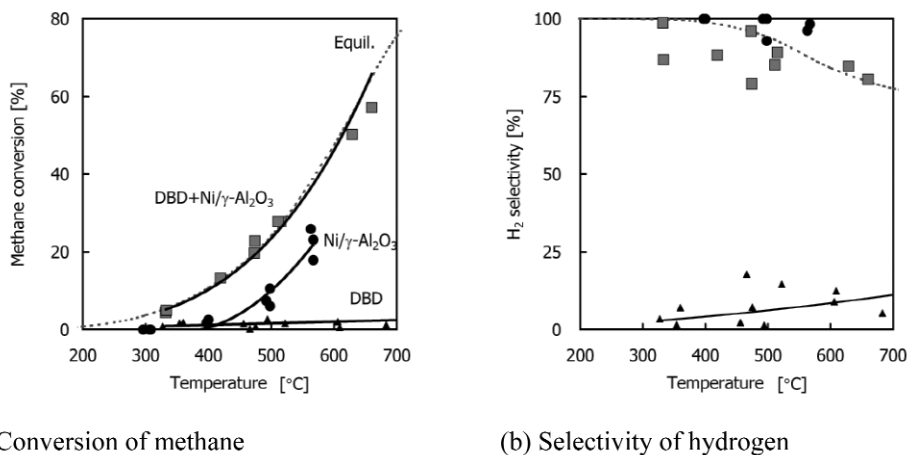


Fig. 7 DBD/catalyst hybrid reactor.

Figure 8a shows an infrared image of a catalyst bed without DBD; panels 8b–8d correspond to the bed temperature with DBD. The reactor is made of sapphire so that the infrared signal transmits to the reactor wall. A caption of each image is accompanied by discharge power, endothermic enthalpy of steam reforming, and temperature of the external electrode measured by thermocouple. The same infrared image is available in color format in ref. [31]. In Fig. 8b, the temperature distribution of the catalyst bed is fairly uniform, and the excess temperature increase is avoided as long as the input power is reasonably minimized. The bed temperature increased remarkably downstream, and the bed temperature also increases much higher than the temperature of external electrode if input energy largely exceeds the endothermic enthalpy of steam reforming (Figs. 8c and 8d). In this operation regime, the heat produced by DBD dominantly promotes a steam reforming reaction. In other words, the net increase in methane conversion is brought by the net increase in the temperature of the catalyst bed [31]. Figure 9 compares methane conversion and hydrogen selectivity obtained using three different conditions. The results clearly show that methane is decomposed only slightly by filamentary barrier discharge because the discharge power was limited in order to avoid an excess temperature increase of the bed (see Fig. 8b), i.e., the specific energy input was less than  $120 \text{ kJ mol}_{\text{CH}_4}^{-1}$  (ca. 13 % of HHV of  $\text{CH}_4$ ). According to Fig. 9, the  $\text{Ni}/\gamma\text{-Al}_2\text{O}_3$  catalyst is more effective than DBD, but results do not reach chemical equilibrium because the space velocity is high ( $\text{GHSV} = 11\,500 \text{ h}^{-1}$ ). On the other hand, the combined result reached equilibrium in the temperature tested. It is important to note that once methane conversion reaches chemical equilibrium, a synergistic effect between DBD and catalyst is no longer expected even if DBD produces excited species because methane conversion is governed by thermodynamic limitation. Note that methane conversion can reach chemical equilibrium without DBD when  $\text{GHSV}$  is  $3600 \text{ h}^{-1}$ : A nonequilibrium plasma does not exhibit a synergistic effect, and DBD seemingly works as a heat source in that operation regime.



**Fig. 8** Temperature distribution of catalyst bed. P: discharge power,  $\Delta Q$ : endothermic enthalpy, GHSV = 11 500 h<sup>-1</sup>, CH<sub>4</sub>/N<sub>2</sub>/H<sub>2</sub>O = 1100/733/1100 cc min<sup>-1</sup>.



**Fig. 9** Methane conversion and hydrogen selectivity vs. catalyst bed temperature measured by infrared camera. GHSV = 11 500 h<sup>-1</sup>, CH<sub>4</sub>/N<sub>2</sub>/H<sub>2</sub>O = 1100/733/2200 cm<sup>3</sup> min<sup>-1</sup> (S/C = 1). Power = 25–120 kJ mol<sub>CH<sub>4</sub></sub><sup>-1</sup>.

Figure 10 schematically presents a potential curve for methane molecule, showing tentative reaction mechanisms in a hybrid reactor [27]. Thermal dissociation of methane to H and CH<sub>3</sub>, for example, follows the ground-state potential curve (II). This process requires a high-temperature heat source (>800 °C) and consumes 4.26 eV dissociation energy per molecule. Methane dissociation by electron impact must follow an upper electronic state that is expressed as a dissociation curve (I). The great benefit of electronic processes is that methane decomposition proceeds independently of temperature and pressure, but its main drawback is that electrons must lose more than twice as much energy as dissociation energy by single collision (9–12 eV >> 4.26 eV). Excess energy fed into methane molecule is dis-

tributed to the kinetic energy of H and CH<sub>3</sub>. Based on our numerical simulation [27], 50 % of electrical energy can be distributed to the dissociation collision to form CH<sub>i</sub> (*i* = 0,1,2,3) and H radicals. However, 60 % of that excited energy must be released for gas heating as an excess input energy: 30 % of the electrical energy fed into methane molecules can be utilized to dissociate the strong C–H bond of methane. This is the reason that the energy cost of plasma fuel conversion is much higher than that for thermal processes. The plasma-enhanced catalytic reaction is explained using a two-step process as shown in Fig. 10 (III). Two vibrational states of methane are produced through inelastic electron collision. Dissociative chemisorption of vibrationally excited methane takes place at lower temperature than that of normal reforming reaction [32]: 35 % of the energy fed into vibrational states, which is inherently wasted in an ordinary DBD reactor, can be utilized in hybrid reactor. In addition, the number density of vibrational species is 10<sup>2</sup> times higher than electrons. Utilization of vibrationally excited methane in plasma catalysis potentially increases the efficiency of the chemical conversion process in a large degree.

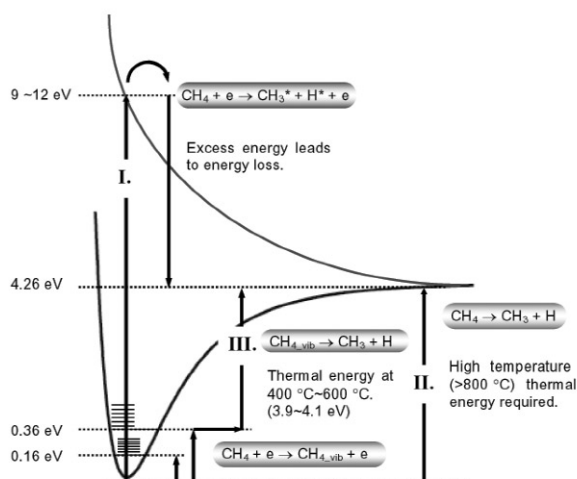


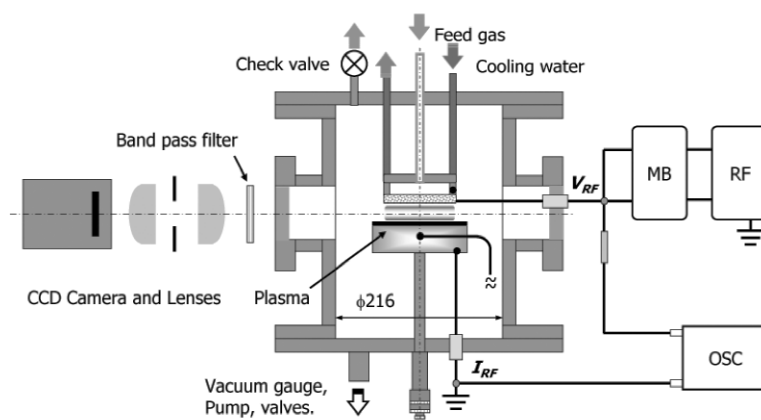
**Fig. 10** Methane activation by thermal energy, electron impact, and their combined effect.

### Deposition of carbon nanotubes in highly collisional cathodic sheath: Atmospheric pressure plasma-enhanced chemical vapor deposition

Atmospheric pressure plasma-enhanced chemical vapor deposition (PECVD) offers great benefits for numerous practical applications. It minimizes the need for vacuum systems and enables the handling of bulky materials in a continuous process. Our group had developed an atmospheric pressure PECVD process for the deposition of carbon nanotubes [33]. In that study, we pointed out that the existence of an energetic cathode region is essential for the growth of carbon nanotubes. However, the quality of nanotubes, such as their diameter, number density, and orientation, was hard to control using an ordinary APGD operated at 10–130 kHz frequencies [34]. The main drawback was that a highly transient plasma is formed intermittently with only a small duty cycle [13,15,20]. In those experiments, effective deposition occurred when the bottom electrode was the momentary cathode where discharge current flows in an interval of ca. 500 ns (see Fig. 2). The duty cycle for effective deposition was between 0.5 and 6.5 % of the cycle time. Furthermore, the cathodic ion sheath, which is essential for the alignment of carbon nanotubes [35], cannot be formed in low-frequency operation. High-frequency operation presents several advantages [4,36]. First, the APGD is regarded as continuous plasma if the operating frequency is sufficiently larger than the inverse of the duration of the current pulse (e.g., 13.56 MHz  $\gg$  1 MHz = (2 × 500 ns)<sup>-1</sup>). In this operating regime, ions are “trapped” in the discharge gap in

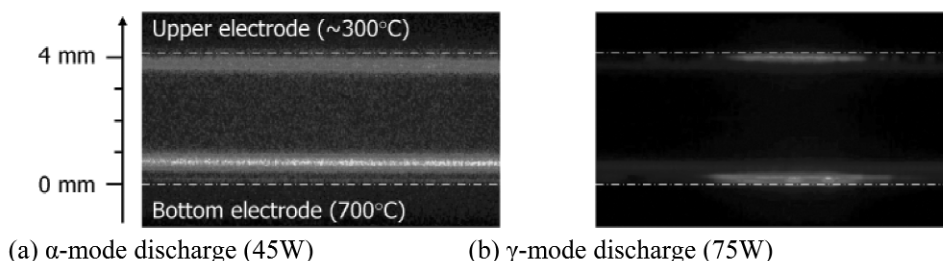
the sense that they do not leave the gap during one discharge pulse, as in the case of the low-frequency APGD. Carbon nanotubes growth might benefit from the quasi-stationary cathodic sheath, where a large potential drop exists. In addition, the operating voltage is remarkably reduced associated with the “ion trapping” which minimizes the formation of a filamentary discharge. In fact, a stable glow discharge can be sustained between two metallic electrodes without a dielectric barrier. The absence of the dielectric barrier might create a large potential drop in the cathodic sheath, whereas ion bombardment should be negligible attributable to the highly collisional ion motion at atmospheric pressure. Although the role of the cathodic sheath for low-pressure PECVD of carbon nanofibers (CNFs) was investigated intensively [37–39], deposition of carbon nanotubes/nanofibers in the highly collisional cathodic sheath is not fully understood: not only the electric field, but also the directionality of the ion movement, the ion energy and ion flux, and the mean free path of particles with respect to length of CNFs might have a significant influence on the growth process [40].

Figure 11 shows an APRFD reactor for carbon nanotube deposition. The RF power source was connected to the upper electrode that is made up of sintered fine metal powder for the uniform gas distribution, whereas the bottom electrode was grounded. Figures 12a and 12b show the spatial emission profile of  $H\alpha$  (656 nm) taken with a band pass filter. Figure 12a shows clearly that intense emission layers are created near the temporary cathode. There is a small asymmetry in the emission intensity that is attributed to the different electrode temperatures and the correspondingly different gas density at the cathode layers. Weak emission exists from the bulk plasma, but its intensity is much lower than that of the cathode layers. The dark space is recognized as a thin dark layer sandwiched by cathode layer and electrode surface. Figure 12b shows that excess input power induced a transition from a uniform  $\alpha$ -mode discharge to non-uniform  $\gamma$ -mode discharge that is characterized by intense plasma spots created in the dark space [41]. Raja et al. performed numerical simulation of high-pressure glow discharges in helium with trace amounts of  $N_2$  [36]. According to their results, an intense cathode layer works as a radical source where ionization and excitation of molecules dominantly takes place. The authors showed that the electron density in cathode layer could reach  $10^{11} \text{ cm}^{-3}$  with a limited amount of nitrogen admixture that efficiently promotes Penning ionization. In our experiment, however, both emission intensity and conduction current decreased by adding a mixture of  $H_2/CH_4$  ( $<1\%$ ), implying that plasma density decreases well below  $10^{11} \text{ cm}^{-3}$ . They also mentioned that maximum electric field (ca.  $4 \text{ kV cm}^{-1}$ ) exists in between the cathode layer and momentary cathode, which corresponds to the dark space shown in Fig. 12a.



**Fig. 11** APRFD reactor. Background pressure:  $10^{-2}$  Torr, Gap: 4 mm.

Gap: 4 mm.



**Fig. 12** Spectral emission distribution of  $H\alpha$ .  $He/H_2/CH_4 = 1000/6/2 \text{ cm}^3 \text{ min}^{-1}$ . 0 mm: substrate surface (700 °C), 4 mm: surface of upper electrode (300 °C). The emission intensity of  $\alpha$ -mode discharge is multiplied by 10 for comparison.

Figure 13 shows CNFs deposited on a silicon substrate at 700 °C. The substrate was coated initially with Cr underlayer (20 nm) and Ni catalyst layer (20 nm) [42]. Figure 13a shows the result of a deposition without plasma. It is important to note that for the deposition condition ( $He/H_2/CH_4 = 1000/4/2 \text{ cm}^3 \text{ min}^{-1}$  at 700 °C) and the substrate used (Ni/Cr-coated silicon wafer), thermal CVD CNF growth would have to be expected. In fact, CNF growth seems to start at a number of nanoparticles, but a clearly developed structure of CNFs is missing. The application of the APRFD plasma engenders to the formation of radical species in the cathode layer that clearly enhances the growth process. Figures 13b–13d show CNFs deposited at different  $H_2/CH_4$  ratios with the APRFD plasma for 5 min. No remarkable difference is apparent in the morphology and growth rate for each case. In addition, CNFs were initially well aligned in each case, but directional randomness increases as CNFs grow. The transmission electron microscopy (TEM) images showed that the catalyst particles on top of CNFs are completely covered by solid carbon. The deposition rate is sufficiently rapid in the APRFD that the catalyst particles rapidly precipitate solid carbon and lose their catalytic activity for further growth. The spectral emission distribution of CH (432 nm) indicates qualitatively that the density of carbon-related radicals is much higher than that of atomic hydrogen in the cathode layer. Further increase in hydrogen was speculated to minimize the contamination of catalyst particle; however, as shown in Fig. 13, it did not make a remarkable difference for the morphology of CNFs. One possible explanation is that atomic hydrogen recombines at a high rate at atmospheric pressure because three-body recombination is the main loss pathway:  $H + H + M \rightarrow H_2 + M$ . Excess amounts of hydrogen might not necessarily result in a higher density of atomic hydrogen, but they might engender a detrimental decrease in plasma density as discussed previously. An increase in etchant radicals is a critical issue for further improvement of atmospheric pressure PECVD used in CNF deposition.

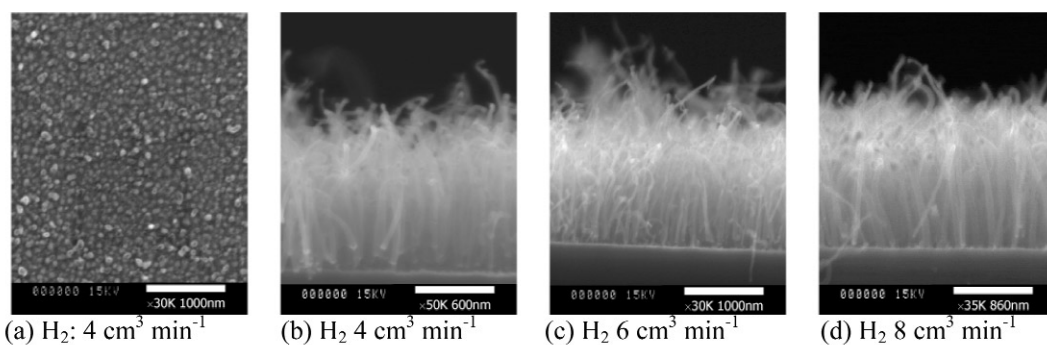


**Fig. 13** SEM images of CNFs obtained at different  $\text{H}_2/\text{CH}_4$  ratios. (a): without plasma, (b–d): plasma with 60 W. Deposition time: 5 min, He:  $1000 \text{ cm}^3 \text{ min}^{-1}$ ,  $\text{CH}_4$ :  $2 \text{ cm}^3 \text{ min}^{-1}$ .

### Creation of microplasma and synthesis of silicon nanoparticles

In this paper, we specifically define microplasma as a nonfilamentary, continuous, high-density ( $N_e \sim 10^{15} \text{ cm}^{-3}$ ), reactive nonequilibrium plasma that is produced at atmospheric pressure. As the reactor dimension approaches the effective  $(pd)_{\min}$  at given conditions, the operating pressure must inevitably increase to sustain self-maintaining discharge. Here,  $(pd)_{\min}$  expresses a Paschen minimum. A typical value is given as  $(pd)_{\min}$  ca. 1 mm Hg-cm in ordinary gases [43]. Unlike transient discharges such as DBD and APGD, microplasma features high-density and extraordinary localized reactive plasmas that provide a unique reaction field in different parameter regions. Our group has explored the new applications into the field of nanoparticle technology and science using such a unique plasma source.

We have developed capacitively coupled very high frequency (VHF) (144 MHz) microplasma shown in Fig. 14. It has a volume of  $1 \mu\text{l}$ . The proposed microplasma reactor offers several advantages over the synthesis of small particles: (1) microplasma under high-frequency operation easily produces supersaturated environment, promoting particle nucleation in the gas phase; (2) high-density plasma might promote ion-induced homogeneous nucleation; (3) charged particles prevent aggregation [44]; (4) particle synthesis from the consecutive reaction is easily optimized with short-residence time reactor (ca. microsecond). In this experiment, TEOS (tetraethoxysilane:  $(\text{C}_2\text{H}_5\text{O})_4\text{Si}$ ) was used as a silicon source for safety. TEOS together with hydrogen ( $1 \text{ cm}^3 \text{ min}^{-1}$ ) was premixed in argon flow ( $1000 \text{ cm}^3 \text{ min}^{-1}$ ) for the synthesis of silicon nanocrystals. Discharge power was maintained at 10–20 W. The microplasma was characterized using emission spectroscopy. The electron density was determined according to the Stark broadening of  $\text{H}_\beta$  (486 nm), and rotational temperature was from the rotational band of CH (432 nm). Both electron density and rotational temperature increased with decreasing internal diameter of capillary tube, showing  $N_e = 3 \times 10^{15} \text{ cm}^{-3}$  and  $T_{\text{rot}} = 1500 \text{ K}$  at 470- $\mu\text{m}$  inner diameter. Rotational temperature also increases with input power, but its electron density remained almost constant with respect to input power.

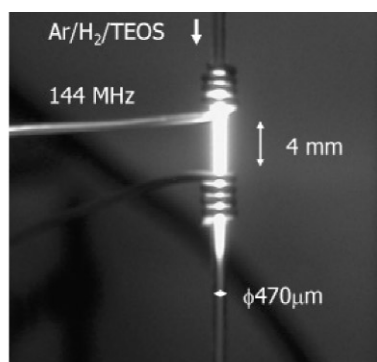


**Fig. 14** Microplasma reactor. Ar:  $1000 \text{ cm}^3 \text{ min}^{-1}$ ,  $\text{H}_2$ : 1000 ppm, TEOS: 5 ppm.

A process starts with the full decomposition of TEOS molecules to form atomic silicon. It is interesting to note that strong emission from atomic silicon was observed at 288 nm and around 250–253 nm, in which neither of them have been identified in TEOS low-pressure plasmas [45]. High-density microplasma would cumulatively be able to dissociate all four strong Si–O bonds; and then ion-induced homogeneous nucleation would take place downstream of the plasma plume. Note that emissions from SiH, SiO, and OH were not observed in the microplasma. The temperature of particles during the growth process is apparently the same level as gas temperature (ca. 1500 K) because of the numerous collisions among clusters/nanoparticles and gas molecules. Figures 15a–15c show SEM images of silicon-related particles deposited at different TEOS concentrations on the TEM grid. Diameters of particles remarkably decrease by minimizing the TEOS concentration, and fine dendritic structures are visible around the edges of the TEM grid. Figure 15d shows the corresponding TEM image of Fig. 15c. The image shows coagulated nanoparticles whose diameters were between 20 and 50 nm. A crystalline structure of silicon was not observed, but a small amount of graphitic structure was detected when the input power was 20 W. Energy-dispersive X-ray (EDX) analyses revealed that the atomic ratios of carbon, silicon, and oxygen of those particles were about C:Si:O = 53:32:15. A weak signal from amorphous silicon was also detected in Raman spectra near  $480 \text{ cm}^{-1}$ , but observation of its Fourier transform infrared (FTIR) absorption spectra confirmed that those particles are mostly silicon oxide, i.e.,  $\text{SiO}_x$ :  $x \approx 0.5$ . TEOS has a single silicon atom that is stabilized with four ethoxy group  $((\text{C}_2\text{H}_5\text{O})_4\text{Si})$  which might inherently produce silicon oxide rather than silicon nanocrystals. The proposed microplasma reactor can synthesize silicon nanocrystals if a correct silicon source is used. We are trying to install facilities that can process tetrachlorosilane instead of TEOS for the synthesis of silicon nanocrystals. Further improvement of the microplasma reactor is being planned.

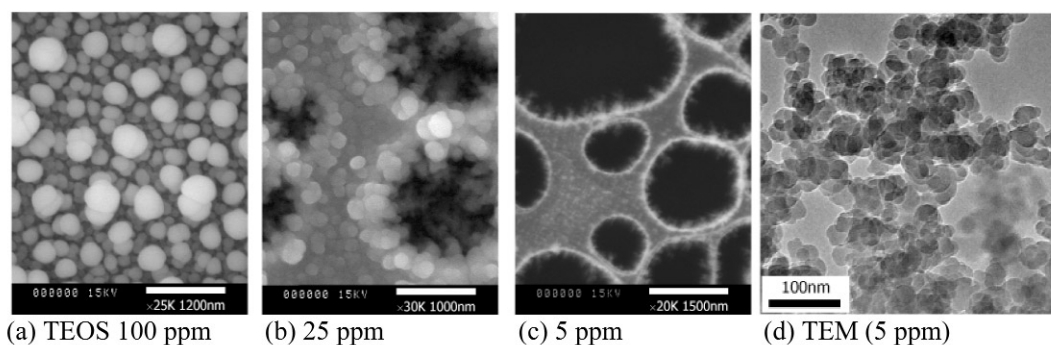


**Fig. 15** TEM images of silicon-related particles deposited at different TEOS concentrations.

### CONCLUDING REMARKS

We discussed fundamental characteristics of filamentary and diffuse barrier discharges. Various applications based on our recent work were overviewed briefly. Industrial application of atmospheric pressure nonequilibrium plasmas will continue to expand into various engineering fields. At the same time, a number of technical challenges have emerged. The major challenge that we would like to emphasize is to suppress the thermalization of nonequilibrium plasmas. Although atmospheric pressure nonequilibrium plasma is recognized as a weakly ionized low-temperature plasma from the fact that its electron temperature is much higher than its gas temperature, electrons are likely to lose their energy through vibrational, rotational, and even momentum transfer collisions. Radical species produced by energetic electrons are the main driving force of chemical conversion processes; however, heat generated by nonequilibrium plasma also accelerates thermal reactions. Modern plasma reactors become compact and are operated at higher frequencies (500–500 kHz). Specifically, in filamentary barrier discharges, increasing power density likely increases the number of filaments per unit area and unit time, whereas electron energy and electron density in each filamentary discharge seem to remain unchanged: Input power is preferably distributed to thermal energy rather than producing radicals. On the other hand, a microplasma developed in our lab can produce high-density reactive nonequilibrium plasma at atmospheric pressure. It is a boundary-dominated plasma; consequently, the heat produced in a microscale reactor is eliminated efficiently through the reactor wall. Therefore, gas temperatures can be limited up to 1500 K for high-density plasma (electron density of ca.  $10^{15} \text{ cm}^{-3}$ ). Although its temperature reaches much higher than room temperature, it is able to provide highly chemical nonequilibrium status. Scientific understanding of the thermodynamic nonequilibrium nature of those plasma sources is strongly needed for further development of this new field of plasma science and technology.

### ACKNOWLEDGMENTS

The authors acknowledge Profs. Joachim Heberlein and Uwe Kortshagen of the University of Minnesota, Minneapolis, Department of Mechanical Engineering, for collaborative research on APRFD and application to the deposition of carbon nanotubes. T.N. would like to thank Dr. Shigeru Kado of the University of Tsukuba for preparation of the reforming catalyst. Projects were granted by New Energy and Industrial Technology Development Organization of Japan (NEDO) and Grants-in-Aid for Scientific Research on the Priority Area of Microplasmas from the Japanese Ministry of Education, Culture, Sports, Science and Technology.

## REFERENCES

1. U. Kogelschatz. *Plasma Chem. Plasma Process.* **23**, 1 (2003).
2. S. Kanazawa, M. Kogoma, T. Moriwaki, S. Okazaki. *J. Phys. D: Appl. Phys.* **21**, 838 (1988).
3. J. R. Roth, J. Rahel, X. Dai, D. M. Sherman. *J. Phys. D: Appl. Phys.* **38**, 555 (2005).
4. J. Park, I. Henins, H. W. Hermann, G. S. Selwyn, R. F. Hicks. *J. Appl. Phys.* **89**, 20 (2001).
5. S. Martin, F. Massines, N. Gherardi, C. Jimenez. *Surf. Coat. Technol.* **177–178**, 693 (2004).
6. <<http://plasma.kue.e.kyoto-u.ac.jp/tokutei429/>>.
7. A. Fridman, A. Chirokov, A. Gutsol. *J. Phys. D: Appl. Phys.* **38**, R1 (2005).
8. E. E. Kunhardt. *IEEE Trans. Plasma Sci.* **28**, 189 (2000).
9. T. Nozaki, Y. Unno, Y. Miyazaki, K. Okazaki. *J. Phys. D: Appl. Phys.* **34**, 2504 (2001).
10. T. Nozaki, Y. Miyazaki, Y. Unno, K. Okazaki. *J. Phys. D: Appl. Phys.* **34**, 3383 (2001).
11. V. I. Gibalov, G. J. Pietsch. *J. Phys. D: Appl. Phys.* **33**, 2618 (2000).
12. K. V. Kozlov, H.-E. Wagner, R. Brandenburg, P. Michel. *J. Phys. D: Appl. Phys.* **34**, 3164 (2001).
13. F. Massines, P. Segur, N. Gherardi, C. Khamphan, A. Ricard. *Surf. Coat. Technol.* **174–175**, 8 (2003).
14. F. Massines, A. Rabehi, P. Decomps, R. B. Gadri, P. Segur, C. Mayoux. *J. Appl. Phys.* **83**, 2950 (1998).
15. L. Mangolini, C. Anderson, J. Heberlein, U. Kortshagen. *J. Phys. D: Appl. Phys.* **37**, 1021 (2004).
16. G. Herzberg. *Molecular Spectra and Molecular Structure, I - Spectra of Diatomic Molecules*, Chap. III, Van Nostrand Reinhold, New York (1950).
17. B. Eliasson, M. Hirth, U. Kogelschatz. *J. Phys. D: Appl. Phys.* **20**, 1421 (1987).
18. J. Luque, M. Kraus, A. Wokaun, K. Haffner, U. Kogelschatz, B. Eliasson. *J. Appl. Phys.* **93**, 4432 (2003).
19. U. Kogelschatz, B. Eliasson, W. Egli. *J. Phys. IV* **7**, 47 (1997).
20. T. Nozaki, Y. Unno, K. Okazaki. *Plasma Sources Sci. Technol.* **11**, 431 (2002).
21. J. M. Cormier, I. Rusu. *J. Phys. D: Appl. Phys.* **34**, 2798 (2001).
22. M. Kraus, W. Egli, K. Haffner, B. Eliasson, U. Kogelschatz, A. Wokaun. *Phys. Chem. Chem. Phys.* **4**, 668 (2002).
23. Y. Li, C.-J. Liu, B. Eliasson, Y. Wang. *Energy Fuels* **16**, 864 (2002).
24. L. Bromberg, D. R. Cohn, A. Rabinovich, J. Heywood. *Int. J. Hydrogen Energy* **26**, 1115 (2001).
25. <<http://www.glidarc-tech.com/>>.
26. O. Mutaf-Yardimci, A. V. Saveliev, A. A. Fridman, L. A. Kennedy. *J. Appl. Phys.* **87**, 1632 (2000).
27. T. Nozaki, N. Muto, S. Kado, K. Okazaki. *Catal. Today* **89**, 57 (2004).
28. T. Nozaki, N. Muto, S. Kado, K. Okazaki. *Catal. Today* **89**, 67 (2004).
29. H. Kim, A. Mizuno, Y. Sakaguchi. *Energy Fuels* **16**, 803 (2002).
30. T. Yamamoto, M. Okubo, K. Hayakawa, K. Kitaura. *IEEE Trans. Ind. Appl.* **37**, 1492 (2001).
31. T. Nozaki, T. Hiroyuki, K. Okazaki. *Energy Fuels* **20**, 339 (2006).
32. L. B. F. Juurlink, P. R. McCabe, R. R. Smith, C. L. DiCologero, A. L. Utz. *Phys. Rev. Lett.* **83**, 868 (1999).
33. T. Nozaki, Y. Kimura, K. Okazaki. *J. Phys. D: Appl. Phys.* **35**, 2779 (2002).
34. T. Nozaki, Y. Kimura, K. Okazaki, S. Kado. *Plasma Processes and Polymers*, p. 477, Wiley-VCH, Weinheim (2004).
35. A. V. Melechko, V. I. Merkulov, T. E. McKnight, M. A. Guillorn, K. L. Klein, D. H. Lowndes, M. L. Simpson. *J. Appl. Phys.* **97**, 041301/1 (2005).
36. X. Yuan, L. L. Raja. *IEEE Trans. Plasma Sci.* **31**, 495 (2003).
37. R. Hatakeyama, G.-H. Jeong, T. Kato, T. Hirata. *J. Appl. Phys.* **96**, 6053 (2004).
38. M. Chhowalla, K. B. K. Teo, C. Ducati, N. L. Rupesinghe, G. A. J. Amaratunga, A. C. Ferrari, D. Roy, J. Robertson, W. I. Milne. *J. Appl. Phys.* **90**, 5308 (2001).

39. D. Hash, D. Bose, T. R. Govindan, M. Meyyappan. *J. Appl. Phys.* **93**, 6284 (2003).
40. T. Nozaki, T. Goto, K. Okazaki, K. Ohnishi, L. Mangolini, J. Heberlein, U. Kortshagen. *J. Appl. Phys.* **99**, 024310-1 (2005).
41. Yu. P. Raizer. *Gas Discharge Physics*, Chap. 13, Springer, Berlin (1991).
42. M. Meyyappan, L. Delzeit, A. Cassell, D. Hash. *Plasma Sources Sci. Technol.* **12**, 205 (2003).
43. A. von Engel. *Ionized Gases*, Oxford University Press, Oxford (1965).
44. A. Bapat, C. Anderson, C. R. Perrey, C. B. Carter, S. A. Campbell. U. Kortshagen. *Plasma Phys. Control. Fusion* **46**, B97 (2004).
45. A. Granier, M. Vervloet, K. Aumaille, C. Vallee. *Plasma Sources Sci. Technol.* **12**, 89 (2003).